Industrial Chemistry & Materials

ROYAL SOCIETY OF CHEMISTRY

PAPER

View Article Online
View Journal

Cite this: DOI: 10.1039/d5im00376h

Dual-dimensional regulation of interface and stress *via* a composite anode for stable gel-based solid-state lithium metal batteries

Yuhao Zhu,[a] Wenhui Bai,[a] Jingjing Ma,[a] Bo Lu,[a] Sheng Chen,[a] Xiaogang Mu,[a] Bo Liu,[a] Weiwei Sun,[b] Yu Han,[b] Shizhao Xiong, [c] Yangyang Liu, [d] Jiajia Li,[e] Huimin Zhao,[e] Xingxing Jiao, *[f] Qingpeng Guo*[b] and Xuanjun Wang*[a]

Solid-state electrolyte lithium (Li) metal batteries have been considered as promising storage devices due to their high energy density, good thermal stability and safety. The key to achieving their superior performance lies in maintaining a stable solid–solid interface. Although applying high pressure is a common strategy to improve interfacial contacts, the generally poor pressure tolerance of the Li metal anode has largely been overlooked by researchers. Under high pressure, the Li anode undergoes significant volume changes and creep, which not only fails to maintain intimate contact but also intensifies interface separation, ultimately leading to performance degradation. Herein, a gel polymer electrolyte (GPE)/Li metal/carbon fiber cloth (CFC) composite anode (G-LiCFC) with high pressure resistance capability was fabricated by the hot-melting method. The G-LiCFC composite anode not only maintains structural integrity under a high pressure of 30 MPa but also contributes to forming an excellent interface with the electrolyte. As a result, the symmetric cells of the G-LiCFC composite anode display stable cycling for 4870 hours at a high areal capacity of 12 mA h cm^{-2}, and the $LiFePO_4$|GPE|LiCFC full cells exhibit excellent cycling performance with no capacity decay after 410 cycles at 0.2 C under a high pressure of 10 MPa.

Keywords: Solid-state electrolyte; Li metal; Carbon fiber cloth/lithium metal composite; Compressive resistance; Interface.

Received 17th December 2025,
Accepted 13th March 2026

DOI: 10.1039/d5im00376h

rsc.li/icm

1 Introduction

With the progress of global carbon neutrality, lithium metal batteries (LMBs) with high capacity and the lowest potential have aroused substantial research interest to improve the energy density for meeting the increasing demands of the society.[1,2] However, the conventional LMBs with liquid electrolytes have safety risks of leakage and ignitability, and the inhomogeneous deposition of lithium metal during cycling would lead to the continuous growth of Li dendrites and poor electrochemical performance, which seriously limit its further development in practical applications.[3–8] Therefore, developing solid-state electrolyte Li metal batteries with good thermal stability and safety is crucial to improve the energy density and solve these issues.[9–13]

The paramount challenge in advancing solid-state lithium metal batteries (SSLMBs) lies in effectively addressing the interfacial instability and substantial volume changes of the Li metal anode under high-capacity cycling conditions.[14–19] This fundamental issue originates from the intrinsic nature of the solid–solid interface, which fundamentally differs from the solid–liquid interface in conventional batteries.[20,21] Unlike liquid electrolytes that can become wet and maintain continuous contact, the physical contact between the solid-state electrolyte and the Li anode is inherently poor, thereby failing to form a stable Li-ion transport channel in a pressure-free state, as illustrated in Fig. 1a.[22] This problem is critically exacerbated by the significant volume change of the Li metal during repeated deposition and stripping, which further aggravates the interface separation and leads to performance degradation.[16,23–26] It is for these intertwined reasons that the

[a] *Zhijian Laboratory, Rocket Force University of Engineering, Xi'an 710025, China. E-mail: wangxj503@sina.com*
[b] *College of Aerospace Science and Engineering, National University of Defense Technology, Changsha, Hunan 410073, China. E-mail: qingpeng.guo@nudt.edu.cn*
[c] *Faculty of Materials Science and Engineering, Kunming University of Science and Technology, Kunming 650093, Yunnan, China*
[d] *School of Instrument Science and Technology, Xi'an Jiaotong University, Xi'an 710049, China*
[e] *Beijing Key Laboratory of Solid State Battery and Energy Storage Process, Institute of Process Engineering, Chinese Academy of Sciences, Beijing, China*
[f] *Research Institute of Frontier Science, Southwest Jiaotong University, Chengdu 610031, China. E-mail: xxjiao@swjtu.edu.cn*

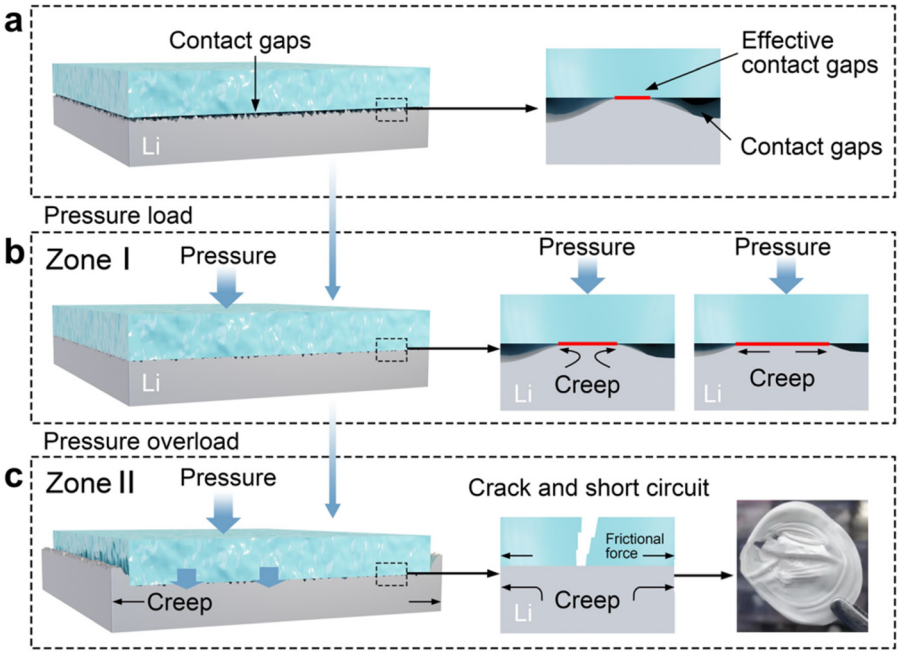

Fig. 1 Schematic of the creep of lithium metal (a) before pressure loading, (b) under external pressure loading and (c) under pressure overloading.

application of a certain external stack pressure is indispensable during the cycling of SSLMBs.[27,28] The applied pressure serves the dual purpose of ensuring good contact among the three solid-state components (cathode, electrolyte, and anode) and accommodating the vertical volume changes of the electrodes during charging and discharging. While applying stack pressure is a necessary strategy to achieve intimate interfacial contact, the intrinsic mechanical properties and limited pressure tolerance of the Li metal anode impose a critical constraint that is often underestimated. The soft and visco-plastic nature of lithium means that its structural stability under pressure cannot be guaranteed, which in turn places a strict upper limit on the pressure that can be practically applied. Recently, Masias *et al.* calculated the Young's modulus of lithium to be 7.82 GPa, the shear modulus was 2.83 GPa, the Poisson's ratio was 0.381, the yield strength was between 0.73 and 0.81 MPa, and the stress index in creep was 6.56.[29] Moreover, Qiang Zhang *et al.* clarified that lithium metal would show an obvious creep under high pressure, and could also produce creep under stress, lower than the yield strength (Fig. 1b). This creep phenomenon becomes particularly hazardous under unconfined conditions, leading to uncontrolled flow or extrusion of lithium metal (Fig. 1c), which significantly increases the risk of internal short circuits. This fundamentally limits the safe operational stack pressure ceiling for practical battery systems, such as pouch cells, typically in the range of 0.4–2 MPa.[30–33]

Therefore, it is imperative to improve the pressure resistance capability of the lithium metal anode electrode and maintain the interfacial stability in the solid-state Li metal batteries during cycling.[34] Herein, the G-LiCFC composite anode was constructed by employing high-strength conductive CFC as the skeletal framework and incorporating a flexible gel polymer electrolyte (GPE). Through this dual-dimensional regulation strategy that combines interface engineering and structural design, the composite lithium anode enhances interfacial compatibility between the Li metal and CFC *via* an aluminum oxide (Al_2O_3) coating. Simultaneously, by leveraging the structural properties of CFC and the viscoelastic characteristics of GPE, a synergistic effect can be achieved through the mechanical support of the carbon fiber skeleton and the interfacial self-adaptability of GPE, enabling dynamic stress balance during Li deposition/stripping. Moreover, the compressive performance of the G-LiCFC anode was evaluated under different pressures to investigate the effect of pressure on the interface between the Li anode and electrolyte. Additionally, the symmetric cells with G-LiCFC composite anode display stable cycling for 4870 hours at a high areal capacity of 12 mA h cm^{-2}, exhibiting excellent high-capacity cycling performance. Full cells assembled with the G-LiCFC composite anode and LFP cathode stably cycled 400 times under 10 MPa. The $LiFePO_4$|GPE|LiCFC full cells exhibit excellent cycling performance with no capacity decay after 410 cycles at 0.2 C under a high pressure of 10 MPa.

2 Results and discussion

The GPE-LiCFC composite (G-LiCFC) was prepared through the hot melting method, as shown in Fig. 2a, in which the molten Li metal can be automatically adsorbed on the CFC after being subjected to lithiophilic treatment with Al_2O_3 coating. Subsequently, the gel polymer electrolyte (GPE) solution was coated on the surface of the LiCFC anode, and then the GPE-LiCFC composite anode (G-LiCFC) was obtained after drying at 100 °C. Moreover, the CFC possesses

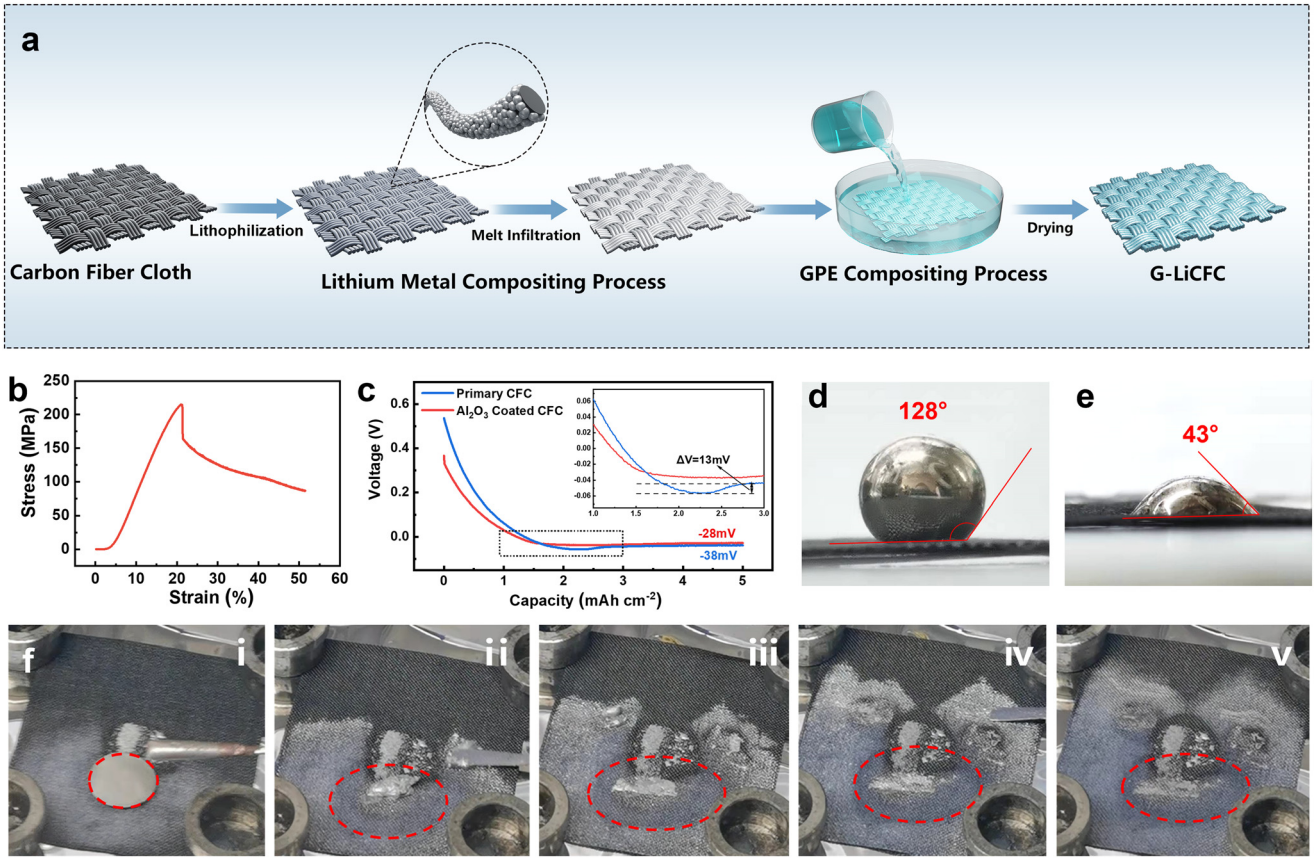

Fig. 2 (a) Schematic of the preparation process of the G-LiCFC composite anode electrode. (b) Stress–strain curve of the carbon fiber cloth. (c) Over-potential of the Li||Cu cell using CFC and Al_2O_3 coated CFC electrodes. (d and e) Contact angles between CFC and molten lithium before and after the lithiophilic treatment, respectively (heat treatment at 500 °C). (f) Optical photograph of the spontaneous diffusion of lithium metal (i–v) in the carbon fiber cloth.

high strength (215.08 MPa) (Fig. 2b) and high specific surface area (110.30 $m^2\ g^{-1}$) (Fig. S2), which is an ideal composite material to support adequate mechanical properties for the Li metal anode. Fig. 2c shows the overpotential of lithium deposition on the CFC before and after Al_2O_3 coating. By comparing the voltage-capacity curves of pristine CFC and the surface-coated modified CFC as deposition substrates, it can be observed that voltage decreases with increasing capacity after deposition on the pristine CFC, showing a distinct voltage trough. After reaching a minimum of −51 mV, it recovers and eventually stabilizes at −38 mV. Notably, after modification with Al_2O_3 coating, the deposition curve undergoes a fundamental change, in which the voltage smoothly decreases to −0.028 V with increasing capacity and remains stable without a distinct voltage trough. This phenomenon, namely the reduction of the nucleation barrier and the disappearance of the nucleation peak, is primarily attributed to the interfacial chemistry developed between the Al_2O_3 coating and lithium. Studies indicate that upon thermal contact, Al_2O_3 undergoes an *in situ* transformation into a Li-rich Li–Al–O interphase.[35] This interphase not only exhibits high lithium-ion conductivity, providing an efficient pathway for ion transport, but also possesses a strong interfacial binding energy with lithium metal. This significantly promotes uniform wetting and intimate contact of lithium, thereby markedly reducing the energy barrier for nucleation. Simultaneously, the stable deposition potential decreased significantly from −38 mV to −28 mV, which further confirms the critical role of the coating-induced interphase in reducing the overall interfacial transport resistance. As shown in Fig. 1d and e, the contact angles are significantly lower after lithiophilic treatment, indicating that the alumina coating enhances the lithiophilicity of the CFC surface. Moreover, the optical photograph shows that the molten Li metal can be spontaneously adsorbed onto the surface of CFC, benefiting from the lithiophilicity of CFC (Fig. 2f).

Based on a comprehensive analysis of electrochemical behavior and morphological observations, the Al_2O_3 coating on the carbon fiber cloth (CFC) demonstrates a profound positive impact on the lithium metal deposition process. Fig. 3a–d show the microstructure of the CFC surface at different stages of the preparation process. The pristine CFC surface has many longitudinal textures, and then becomes very smooth after coating on the CFC with Al_2O_3. LiCFC can be obtained by combining the coated CFC with Li metal, as shown in Fig. 3c, in which the Li metal is relatively uniformly coated on the CFC surface. This proves that the Al_2O_3 coated CFC has good affinity

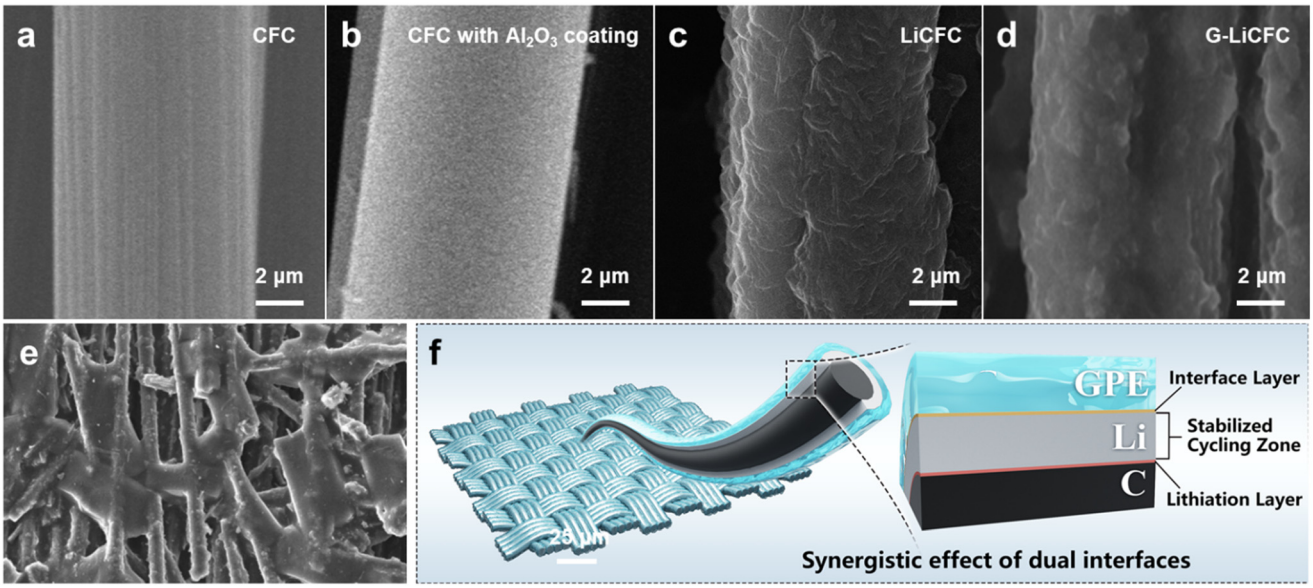

Fig. 3 SEM images of (a) primary CFC, (b) CFC with Al_2O_3 coating, (c) LiCFC and (d) G-LiCFC. (e) SEM image of Li infiltration on the primary CFC. (f) Schematic of the interface inside the G-LiCFC composite anode.

for Li metal and plays a role in the electrodeposition process. Subsequently, GPE was modified on the LiCFC surface (Fig. 3d), and it can be seen that the GPE was uniformly coated on the LiCFC surface. In contrast, pristine CFCs do not have a good affinity for lithium metal; therefore, lithium metal cannot be uniformly deposited on CFCs (Fig. 3e). Thus, the G-LiCFC composite anode forms a dual-interface structure in Fig. 3f, in which lithium metal is located between the carbon fiber and GPE, and the two contact interfaces are a lithiophilic interface and a LiF-rich interface, respectively. The protective properties of lithium metal at these two interfaces help to form a stable cycling region.

To evaluate the compressive property of the G-LiCFC composite anode, the pure Li sheet and G-LiCFC composite anode were investigated under different high pressures. Fig. 4a and b shows optical photograph of the Li sheet and G-LiCFC composite anode under different pressures. It is found that the lithium sheet shows no obvious deformation when the pressure is up to 5.19 MPa, and the change rates of its diameter and thickness are 3.74% and 3.00%, while the change rates of the diameter and thickness of G-LiCFC are 2.00% and 2.00%, respectively (Fig. 4c and d). With the gradual increase in pressure, the deformation of the lithium sheet tends to be serious. When the pressure is up to 17.79 MPa, the edge of lithium metal is seriously wrinkled, cracked and damaged and the change rate of diameter and thickness reached to 37.03% and 46.20%, which is attributed to the fact that lithium metal with a low yield strength undergoes severe deformation due to creeping under high pressure. In contrast, the deformation of composite lithium metal almost has no obvious change with diameter change rate of 8.27% even under the pressure of 30 MPa (Fig. S3). However, the change rate of G-LiCFC in the thickness direction is relatively high, mainly due to certain voids inside G-LiCFC, which are squeezed together when subjected to external pressure, resulting in a large change rate in the direction of thickness. The results indicate that the G-LiCFC composite anode has good compressive performance, which is because the Li metal is bound in the network composed of carbon fibers (Fig. 4e). Moreover, when the pressure is applied on the G-LiCFC composite anode, the pressure is distributed to the carbon fibers with high tensile strength, which endows the G-LiCFC composite anode with excellent compressive performance to maintain structural stability even under high pressure.

In order to investigate the effect of different pressures on the interface between the Li composite anode and GPE, the Li|GPE|Li and G-LiCFC|GPE|G-LiCFC symmetrical cells were tested using electrochemical impedance spectroscopy, as shown in Fig. 5. The symmetrical cells were assembled according to the sequence of stainless steel sheet, lithium sheet, electrolyte, lithium sheet, and stainless steel sheet, and the battery is encapsulated by an aluminum film (Fig. 5a). Subsequently, the symmetrical cells were placed between stainless steel plates and subjected to different pressures (Fig. 5b).

For the symmetric cell with bare Li metal anodes, the Nyquist plots under different pressures exhibit a regular semicircular shape (Fig. 5c). The fitted interfacial impedance (R_{ct}) reveals a distinct two-stage response to increasing pressure (Fig. 5d). Initially, in what is defined as the interface improvement zone (zone I), the impedance decreases sharply due to enhanced physical contact. Upon reaching a critical pressure, the system transitions into the material-bearing zone (zone II), where the impedance reduction rate diminishes markedly. In this high-pressure regime, the stress is transmitted directly into the bulk Li metal. Given its low yield strength, the Li anode undergoes peristaltic deformation, which not only hampers further impedance reduction but also poses a risk of internal short circuits.

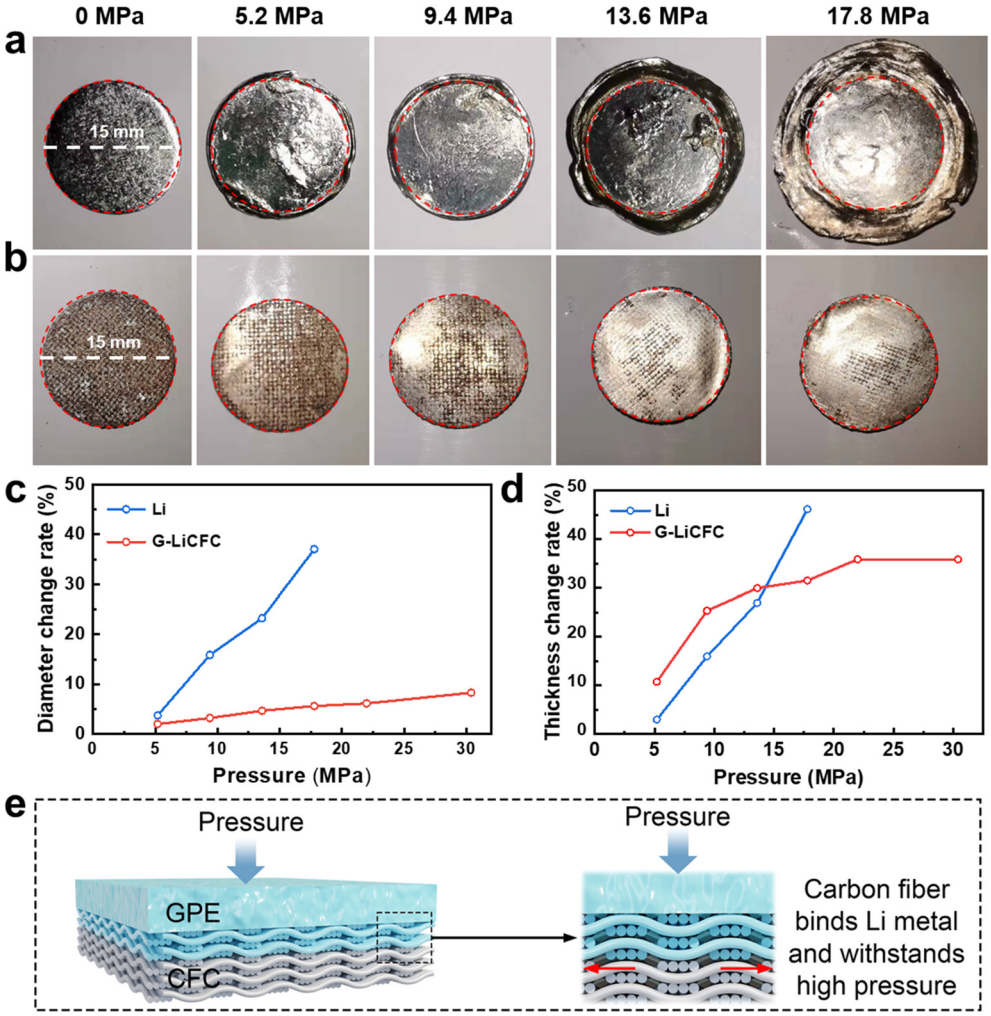

Fig. 4 Deformation of the Li sheet (a) and G-LiCFC composite (b) anode electrode with different pressures. The red dashed circle in each image represents a diameter of 15 mm, serving as a scale reference. (c) Diameter change rate and (d) thickness change rate of the Li sheet and G-LiCFC composite anode electrode under different pressures. (e) Schematic of the change of the Li metal inside the G-LiCFC composite anode electrode before and after external pressure.

In contrast, the G-LiCFC composite anode demonstrates a superior and distinct pressure response (Fig. 5e and f). While its impedance-pressure relationship also conforms to the two-zone model, the transition is more pronounced. Most notably, in zone II, the interfacial impedance of the G-LiCFC anode stabilizes and shows negligible change even when the pressure is increased to 30 MPa. This exceptional performance is attributed to its composite architecture, in which the Li metal is confined within a mechanically robust carbon fiber cloth (CFC) network. When an external pressure is applied, the stress is predominantly borne by the high-tensile-strength CFC skeleton, which shields the soft Li from detrimental deformation.

Collectively, these results unequivocally demonstrate that the G-LiCFC composite anode effectively maintains structural and interfacial integrity at the GPE interface under extreme pressures up to 30 MPa, overcoming a fundamental limitation of bare Li metal.

The symmetric cell with Li anode and G-LiCFC composite anode was used to investigate the cycling stability under high deposition capacity. As shown in Fig. 6a, the G-LiCFC|GPE|G-LiCFC symmetric cell maintains a stable voltage of 67 mV and achieves a stable cycle life of 350 hours at a relatively high current density of 0.5 mA cm^{-2} and a capacity of 0.25 mA h cm^{-2}. As shown in Fig. S4, the LiCFC|GPE|LiCFC symmetric cells maintain a stable polarization voltage even at a current density of 1.4 mA cm^{-2}, while as the current density increases to 1.6 mA cm^{-2}, the polarization voltage of PPE rises significantly, exhibiting the formation of dead Li or dendrites, or loss of contact at the electrode interfaces. In contrast, the Li|GPE|Li symmetric cell exhibits an unstable and flaring-shaped voltage profile with the voltage climbing to 0.6 V at 275 hours and failing rapidly in subsequent cycles. When the G-LiCFC|GPE|G-LiCFC symmetric cell was cycled at an ultra-high capacity of 12 mA h cm^{-2} (0.2 mA cm^{-2}) (Fig. 6b), the overpotential of the G-LiCFC composite anode remained between 15–20 mV with a

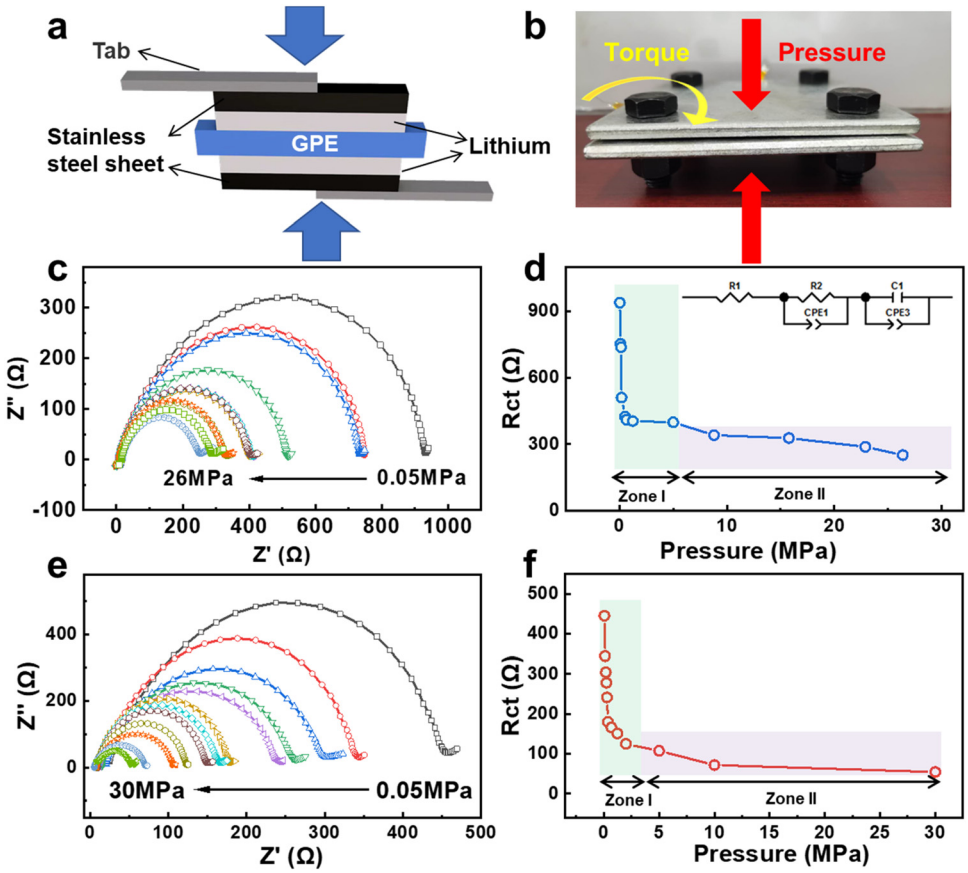

Fig. 5 Impedance variation of the Li plate and G-LiCFC composite negative electrode under different pressures. (a) Schematic of the pressure test battery assembly. (b) Schematic of the relationship between the torque force and longitudinal pressures. (c) Impedance spectra of the Li slices under different pressures. (d) Relation curve between the interfacial impedance and pressure of Li wafer. (e) Impedance spectra of the G-LiCFC composite anode electrode at different pressures. (f) Relation curve between the interfacial impedance and pressure of the G-LiCFC composite anode electrode.

stable cycle life of 4870 hours, demonstrating excellent high-capacity cycling capability, while the Li|GPE|Li symmetric cell short-circuited after only 733 hours. The superior high-capacity cycling performance of the G-LiCFC composite anode is primarily attributed to its stable cycling structure under dual interface protection.

Furthermore, the microscopic morphology of the G-LiCFC composite anode and Li anode was conducted after the first cycle. Fig. 6c and S5 show the SEM image of the cycled pristine Li anode, in which very rough and dendritic morphology was observed. The SEM images of the high Li-loading state G-LiCFC composite anode (Fig. 6d and e) show Li metal deposited around the CFC with no observation of uneven Li deposition, which indicates that Li metal can be uniformly deposited and stripped along the thickness direction. This suggests that the structure of the G-LiCFC composite anode is highly reversible, and the high specific surface area of CFC is beneficial for the high Li-deposition.

Moreover, X-ray photoelectron spectroscopy (XPS) was conducted to demonstrate that the LiF content at the LiCFC/GPE interface after cycling was significantly higher than that of the bare lithium anode under the same conditions (Fig. S6). This result directly supports the existence and chemical properties of the LiF-rich interface. X-ray microscopy (XRM) was used to characterize the three-dimensional spatial distribution of Li metal inside the G-LiCFC composite anode. Fig. 6f and g are XRM images along the *x*-axis and *z*-axis (cross-sectional direction), respectively, where the CFC (black), electrolyte phase (yellow), and Li metal phase (red) are distinguished based on material density differences. Fig. 6h and i display the original cross-sectional image and the corresponding reconstructed three-dimensional structure. Based on these XRM images, it can be observed that the GPE encapsulates the CFC, and Li metal is uniformly distributed between the CFC and the GPE and primarily deposited on the outer surface of the GPE layer surrounding the CFC. Therefore, the G-LiCFC composite anode, with the protection of this dual interface, could improve high deposition capacity and maintain structural integrity during cycling.

To further verify the electrochemical performance of the G-LiCFC composite anode applied to solid-state batteries, the $LiFePO_4$|GPE|G-LiCFC (Fig. 7a) and $LiFePO_4$|GPE|Li full cells were assembled and tested at 0.2 C under a pressure of 10 MPa. The $LiFePO_4$|GPE|Li full cell exhibits an initial discharged

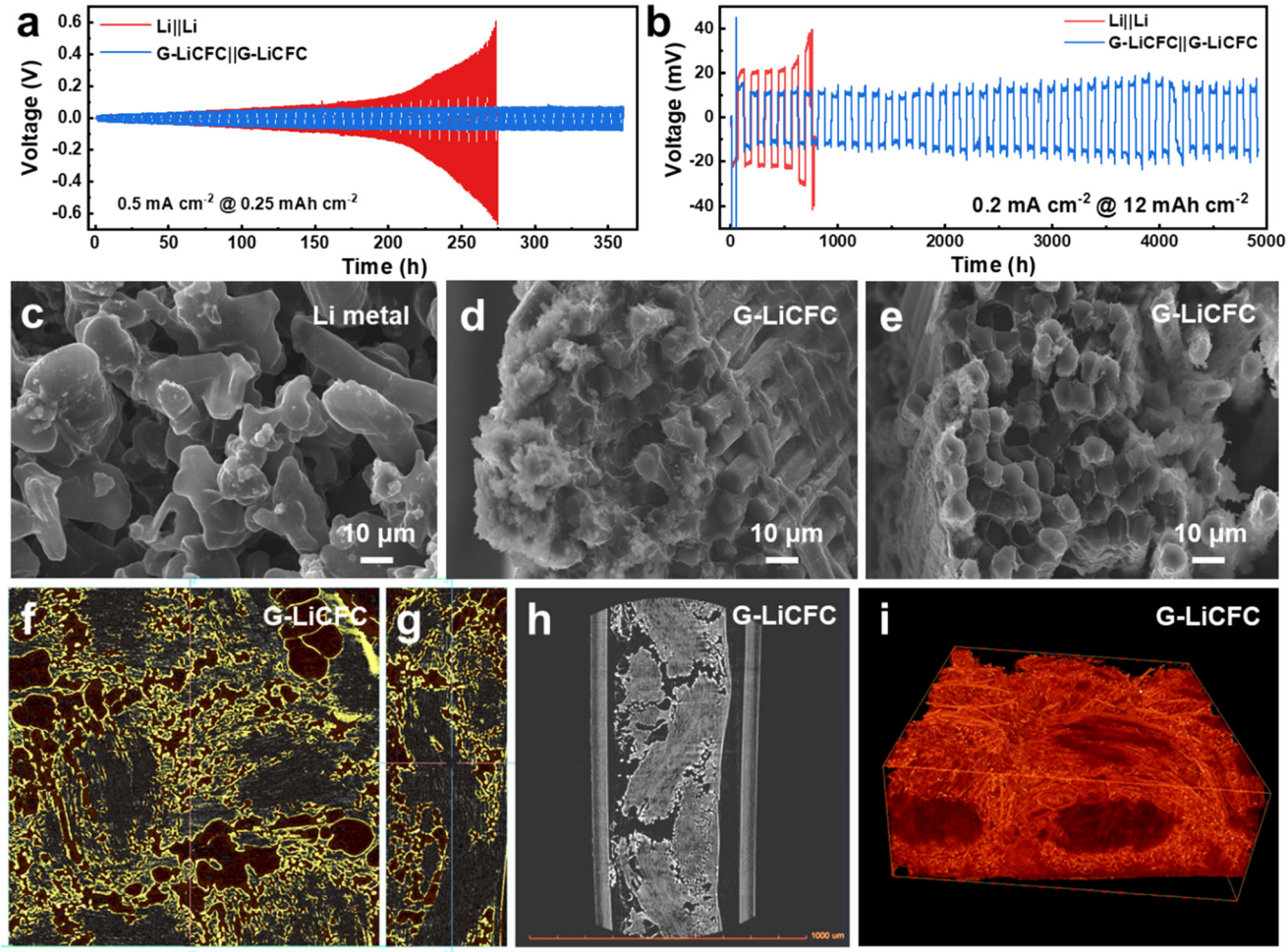

Fig. 6 Stability of the electrochemical plating-stripping process of the Li|GPE|Li and G-LiCFC|GPE|G-LiCFC symmetric cells at current densities of (a) 0.5 mA cm^{-2} and (b) 0.2 mA cm^{-2}. (c and d) SEM images of the Li metal and G-LiCFC anodes, respectively, under a high capacity of 12 mA h cm^{-2}. (e) SEM images of the G-LiCFC anode under a low capacity of 0.25 mA h cm^{-2}. XRM images of the (f) surface (black: CFC; yellow: electrolyte phase; and red: metallic Li phase), (g) cross-section, (h) primary cross-section and (i) 3D reconstruction of the G-LiCFC composite anode after 1 cycle.

capacity of only 23.3 mA h g^{-1} and the Coulomb efficiency decreases rapidly, eventually leading to failure after only 11 cycles (Fig. 7b and c). This poor performance originated from the continuous creep and plastic deformation of bare Li metal under high pressure, which led to an unstable electrode/electrolyte interface, repeated rupture/reformation of the SEI, and irreversible active loss of Li. These processes significantly increased the interfacial impedance and blocked ion transport. In sharp contrast, the $LiFePO_4$|GPE|G-LiCFC full cell displays an initial discharged capacity of 111.9 mA h g^{-1}, which presents an excellent cycling performance with 133.0 mA h g^{-1} after 400 cycles (Fig. 7d). Moreover, Fig. S7 clearly shows the rate performance of the $LiFePO_4$|GPE|G-LiCFC cell, cycled 5 times at each current density. The $LiFePO_4$|GPE|G-LiCFC cell exhibits a reversible capacity of about 95.9 mA h g^{-1} at 0.75 C. The $LiFePO_4$|GPE|G-LiCFC full cell exhibited good cycling performance with 125.3 mA h g^{-1} after 200 cycles (Fig. S8) under a pressure of 2 MPa. This superior stability is attributed to the synergistic effect of dual interfaces and mechanical support from the carbon scaffold: the *in situ*-formed LiF-rich interphase at the Li/electrolyte interface provided high ionic conductivity while electronically insulating, significantly reducing interfacial resistance; concurrently, the Al_2O_3-derived lithiophilic interphase guided uniform Li deposition within the scaffold, suppressing dendrite growth. The rigid carbon fiber structure effectively restrained Li deformation under pressure, maintaining interfacial integrity. This mechanistic understanding is directly corroborated by the post-cycling analysis (Fig. 7e and f), which visually shows severe deformation of the bare Li anode, whereas the G-LiCFC composite maintained its structural integrity after 400 cycles, confirming its dual mechanical and electrochemical advantages.

3 Conclusion

In summary, a G-LiCFC composite anode was successfully fabricated through meticulous interface engineering. The design features a lithiophilic Al_2O_3 coating on the CFC to facilitate favorable Li deposition and a subsequent GPE coating, which together create a unique dual-interface

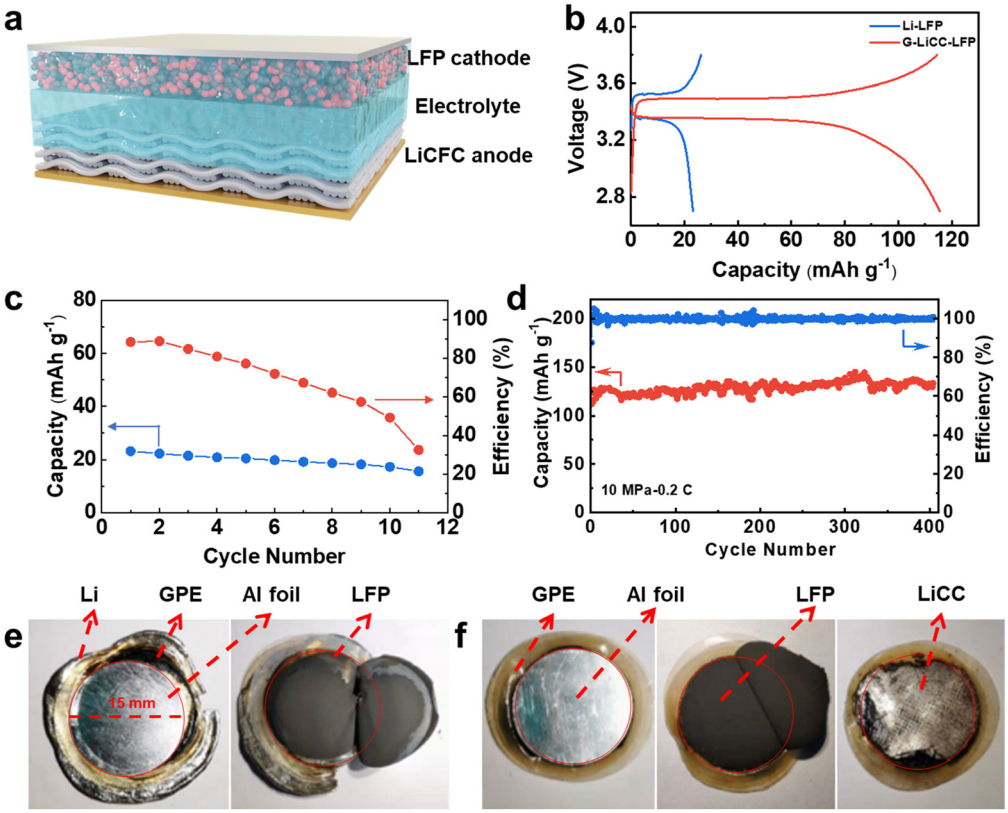

Fig. 7 Electrochemical performance of the $LiFePO_4$|GPE|G-LiCFC solid state batteries. (a) Schematic of the full battery assembly. (b) Galvanostatic charge–discharge profiles of the $LiFePO_4$|GPE|Li and $LiFePO_4$|GPE|G-LiCFC full cells. Cycling performance of the (c) $LiFePO_4$|GPE|Li and (d) $LiFePO_4$|GPE|G-LiCFC full cells. (e and f) The optical photos of the (e) $LiFePO_4$|GPE|Li and (f) $LiFePO_4$|GPE|G-LiCFC full cell electrodes after cycling. The red dashed circle in each image represents a diameter of 15 mm, serving as a scale reference.

architecture. In this structure, the Li metal is confined between the carbon fiber (forming a lithiophilic interface) and the GPE (forming a LiF-rich interface), establishing a stable cycling region that effectively protects the Li metal. Complementing this interfacial stability, the pressure-dependent electrochemical response reveals a characteristic two-regime behavior in the interfacial impedance: an interface improvement zone (zone I) at lower pressures, where impedance decreases sharply, and a material-bearing zone (zone II) at higher pressures. Crucially, in zone II, the Li metal anchored within the robust 3D CFC network benefits from effective load distribution due to the high tensile strength of the framework, which maintains interfacial stability and prevents the detrimental deformation observed in bare Li anodes. The synergy between the stabilized interfaces and the mechanically reinforcing structure is the cornerstone of the exceptional electrochemical performance. This is demonstrated by the G-LiCFC-based symmetric cell achieving stable operation for 4870 hours at a high areal capacity of 12 mA h cm^{-2}, and the corresponding $LiFePO_4$|GPE|G-LiCFC full cell retaining a high capacity of 133.0 mA h g^{-1} after 400 cycles at 10 MPa. By simultaneously ensuring interfacial integrity, homogeneous Li deposition, and structural resilience, the G-LiCFC composite anode paves a promising path toward practical high-energy-density solid-state batteries.

Building on these findings, while the G-LiCFC composite anode demonstrates remarkable pressure tolerance and cycling stability in the $LiFePO_4$/GPE model system, its general applicability across different battery architectures requires further validation. Future studies will prioritize assessing the compatibility of this anode with high-voltage cathodes (*e.g.*, NMC and $LiCoO_2$) and other solid-state electrolytes, particularly sulfide-based and oxide-based ceramics, to broaden its potential application scope. Furthermore, it is acknowledged that the incorporation of carbon fiber cloth, while enhancing mechanical robustness, introduces challenges to the overall energy density and cost-effectiveness of full cells. Subsequent efforts will focus on structural optimization of the scaffold, such as employing thinner, more porous, and lightweight carbon materials, coupled with precise control of lithium loading, to improve energy density and cost efficiency without compromising interfacial stability. Additionally, process development and system integration toward scalable production will be essential to advance the practical adoption of this material.

4 Experimental part

4.1 Preparation of the G-LiCFC composite anode

The carbon fiber cloth (Taiwan Tanneng WOS1009) was impregnated with a pre-dispersed AlOOH aquasol (2 wt%),

dried, and subsequently heat-treated at 450 °C for 2 hours in air to obtain an alumina-coated carbon fiber cloth. The treated carbon fiber cloth was placed on a flat heater and heated to 280 °C. After that, the lithium sheet (Wuxi Xinneng Lithium Industry Co., Ltd., battery-grade purity) was put on the surface of the carbon fiber cloth (the amount of lithium added per square centimeter of the carbon fiber cloth is controlled at about 0.01 g). When the lithium sheet was melted, it was necessary to remove the oxide layer on the surface of the molten lithium with tweezers, and the molten lithium can automatically and evenly diffuse on the carbon fiber cloth. After cooling, a lithium-carbon fiber cloth composite (LiCFC) was obtained. Poly(vinylidene fluoride-*co*-hexafluoropropylene) (PVDF-HFP) (ARKEMA, France, battery grade purity) was completely dissolved in NMP (Tianjin Kemio Chemical Reagent Center, analytical grade) to obtain a transparent solution, and then lithium salt (LiTFSI, Sigma-Aldrich, 99.95%) and ionic liquid (EMITFSI, Lanzhou Institute of Physics and Chemistry, 99.9%) were added into the above solution ($M_{\text{PVDF-HFP}}:M_{\text{LiTFSI}}:M_{\text{EMITFSI}} = 5:5:7$). Subsequently, the LiCFC put on an evaporating dish was coated with the electrolyte solution, in which the gel electrolyte solution was added at an amount of 0.117 g cm^{-2}. Then, it was dried in a vacuum oven at 100 °C for 48 h, taken out and cut into 15 mm discs to obtain a G-LiCFC composite anode electrode. The above operations were all carried out in a glove box or drying room. Based on the weighing of multiple batches of samples, the pristine carbon fiber cloth with a diameter of 15 mm had an average mass of 21.6 mg. After molten lithium infiltration, the average mass of the LiCFC intermediate increased to 38.9 mg. The mass difference of 17.3 mg corresponds to the mass of the loaded metallic lithium. Following coating and drying, the final G-LiCFC composite electrode exhibited an average mass of 66.7 mg. The relative standard deviations for both the total electrode mass and the lithium loading across different batches were less than 5%, indicating good reproducibility of the preparation process. Using the mass data above and the theoretical specific capacity of metallic lithium (3860 mA h g^{-1}), the theoretical capacity contributed by the loaded lithium was calculated to be 66.8 mA h. Consequently, the theoretical gravimetric capacity of the composite anode is 66.8 mA h divided by 66.7 mg, approximately 1002.6 mA h g^{-1}. Based on its geometric area of 1.76 cm^2, the theoretical areal capacity is approximately 38 mA h cm^{-2}.

4.2 Preparation of the electrolyte

PVDF-HFP was completely dissolved in butanone (Tianjin Kemeiou Chemical Reagent Center, analytical grade) to obtain a clear solution, and then lithium salt (LiTFSI), ionic liquid (EMITFSI) and solid electrolyte powder (LLZO Shenzhen Kejing, battery grade) were added to the above solution ($M_{\text{PVDF}}:M_{\text{LiTFSI}}:M_{\text{EMITFSI}}:M_{\text{LLZO}} = 5:5:7:5$). The mixed solution was sealed and ground for 1 h, then poured into stainless steel molds, and vacuum-dried at 60 °C for 12 hours to obtain a gel polymer membrane. The thickness of the film was about 30 μm. This gel polymer film is used as an electrolyte to assemble solid-state batteries in this study.

4.3 Preparation of the positive electrode sheet

$LiFePO_4$ powder (Tianjin Zhongpoly Co., Ltd., battery grade), super P (Shanghai Huiping Chemical Co., Ltd., battery grade) and PVDF were mixed in NMP solvent with a mass ratio of 8 : 1 : 1. The slurry was then coated on an Al/C foil and vacuum dried at 110 °C for 12 h. Finally, the cathode electrode was cut into 15 mm diameter discs. The average mass loading of the $LiFePO_4$ cathode is about 1.6 mg cm^{-2}.

4.4 Material characterization

The microstructure of the composite electrolyte was characterized by scanning electron microscopy (SEM, Hitachi S-4800). The tensile strength of the carbon fiber cloth was measured using a universal testing machine (CMT6103, MTS Industrial Systems). Its specific surface area was determined *via* Brunauer–Emmett–Teller (BET) measurements on a V-Sorb 2800 analyzer. The surface molecular structure and elemental valence states of the G-LiCFC composite anode were analyzed by X-ray photoelectron spectroscopy (XPS, VG ESCALAB 200i XL). Furthermore, the internal structure of the anode was examined using an X-ray microscope (XRM, Versa 520, Carl Zeiss), with the sample being wrapped and sealed in a polyimide film for the measurement. All electrochemical performance tests were conducted at 60 °C.

4.5 Electrochemical measurements

The full cells were assembled in a CR2032-type coin cell configuration. A $LiFePO_4$ cathode and the G-LiCFC composite anode was used as the working and counter electrodes, respectively. Prior to assembly, the current collector-facing side of the G-LiCFC anode was lightly abraded to expose the underlying carbon cloth or lithium metal, thereby ensuring efficient electron transport. The electrodes were separated by the gel polymer film.

The electrochemical performance of the cells was then tested on a LAND CT2001A system to assess their cyclability. Electrochemical impedance spectroscopy was performed on a Princeton Versa STAT electrochemical workstation with scan frequencies ranging from 10^{-1} to 10^5 Hz.

4.6 Assembly and pressure control of pressurized solid-state batteries

The symmetric battery was assembled by stacking the stainless steel sheet, lithium sheet, electrolyte, lithium sheet, and stainless steel sheet in that order, using aluminum-plastic film to encapsulate the battery and using two stainless steel plates (Fig. S1a and b) to seal. The battery was sandwiched in the middle (for assembling a full battery, just replace one of the lithium sheets with a cathode electrode) and fastened with screws. Moreover, the applied pressure was controlled by tuning the tightness of the screws and the screw was operated with a

torque wrench. The greater the torque required to turn the screw, the greater the longitudinal pressure exerted by the screw. The torque was recorded with a digital torque wrench, and the pressure in the pressure die was measured with a high-precision pressure sensor. Fig. S1c shows the relationship between the measured torque and pressure. The torque force is positively correlated with the pressure (pressure). According to the fitting of the experimental test points, the relationship between the pressure F and the torque force T is $F = 543.09 + 739.49T$. Combined with the area of the battery pole piece, the pressure P on the pole piece and the torque force T, the relationship is $P = 3.0857 + 4.2016T$. To ensure the stability of the mechanical constraint throughout the test, a periodic monitoring and correction protocol was implemented. At defined intervals, the applied torque was re-measured and recalibrated to promptly restore the pressure to the specified target value. This procedure ensured that the average stack pressure experienced by the cell remained within the target range for the duration of the cycling experiment. It should be noted that this calibration relationship is an empirical model derived from fitting data within a limited torque range (>0.5 N m). Its non-zero intercept reflects a mathematical extrapolation beyond the data range rather than a directly measurable physical pressure. Therefore, this model is suitable for describing trends in the higher pressure regime (>4 MPa). For the very low pressures involved in this study, an independent direct loading method, verified in real-time by a high-precision sensor, was employed. These two approaches are complementary within their respective applicable ranges, collectively ensuring the accuracy and reliability of the experimental conditions across the entire pressure spectrum. In the high-pressure test, the battery is mainly assembled through this pressure test mold, and the pressure applied to the battery is controlled by the torque force.

Author contributions

Yuhao Zhu: conceptualization, methodology, investigation, formal analysis, data curation, writing – original draft, and visualization. Wenhui Bai: investigation, validation, and data curation. Jingjing Ma: methodology, formal analysis, and investigation. Bo Lu: investigation and data curation. Sheng Chen: investigation and formal analysis. Xiaogang Mu: investigation and data curation. Bo Liu: investigation and validation. Weiwei Sun: resources, investigation, and formal analysis. Yu Han: resources and investigation. Shizhao Xiong: software, formal analysis, and investigation. Yangyang Liu: investigation and validation. Jiajia Li: investigation and data curation. Huimin Zhao: investigation. Xingxing Jiao: supervision, writing – review and editing, and funding acquisition. Qingpeng Guo: conceptualization, supervision, writing – review and editing, and funding acquisition. Xuanjun Wang: conceptualization, supervision, writing – review and editing, funding acquisition, and project administration.

Conflicts of interest

The authors declare no conflicts of interest.

Data availability

The data that support the findings of this study are available from the corresponding author upon reasonable request.

Supplementary information (SI) is available. See DOI: https://doi.org/10.1039/d5im00376h.

Acknowledgements

This work was financially supported by the Natural Science Basic Research Program of Shaanxi (No. 2024JC-YBQN-0127). The authors also gratefully acknowledge the financial support from the Postdoctoral Fellowship Program of CPSF (No. GZC20233564), the Postdoctoral Fellowship Program (Grade C) of China Postdoctoral Science Foundation (No. GZC20241408), Self-deployment Fund of State Key Laboratory of Mesoscience and Process Engineering (No. MESO-25-E05) and the China Postdoctoral Science Foundation (No. 2025M770051).

References

1 Z. Wei, D. Yuan, X. Yuan, Y. Zhang, J. Ma, S. Zhang and H. Zhang, Formulation principles and synergistic effects of high-voltage electrolytes, *Chem. Soc. Rev.*, 2025, **54**, 3775–3818.
2 A. Daali, R. Amine, W. Otieno, G.-L. Xu and K. Amine, Strategies to enable microsized alloy anodes for high-energy and long-life alkali-ion batteries, *Ind. Chem. Mater.*, 2024, **2**, 489–513.
3 X. Xu, X. Jiao, O. O. Kapitanova, J. Wang, V. S. Volkov, Y. Liu and S. Xiong, Diffusion limited current density: A watershed in electrodeposition of lithium metal anode, *Adv. Energy Mater.*, 2022, **12**, 2200244.
4 X. Xu, Y. Liu, J. Y. Hwang, O. O. Kapitanova, Z. Song, Y. K. Sun, A. Matic and S. Xiong, Role of Li-ion depletion on electrode surface: Underlying mechanism for electrodeposition behavior of lithium metal anode, *Adv. Energy Mater.*, 2020, **10**, 2002390.
5 X. R. Chen, Y. X. Yao, C. Yan, R. Zhang, X. B. Cheng and Q. Zhang, A diffusion–reaction competition mechanism to tailor lithium deposition for lithium-metal batteries, *Angew. Chem., Int. Ed.*, 2020, **59**, 7743–7747.
6 N. Zhang, T. Hou, G. Han, Y. Yu, H. Xu and Y. Huang, Smart batteries: Materials, monitoring, and artificial intelligence, *Chem. Soc. Rev.*, 2025, **54**, 10006–10139.
7 Y. Lu, X. Zhang, Y. Wu, H. Cheng and Y. Lu, In situ polymerization of fluorinated electrolytes for high-voltage and long-cycling solid-state lithium metal batteries, *Ind. Chem. Mater.*, 2025, **3**, 151–177.
8 Y. Chen, G. Zhao, J. Dong, J. Wang, D. Dong, Z. Li, M. Zhao, Z. Shi and Z. Niu, Green recovery of all-solid-state sodium-ion batteries/lithium-ion batteries by ionic liquids, deep eutectic solvents and low-melting mixture solvents, *Ind. Chem. Mater.*, 2025, **3**, 464–474.

9 W. Lei, X. Jiao, S. Yang, F. B. Ajdari, M. Salavati-Niasari, Y. Feng, J. Yin, G. Ungar and J. Song, Temperature and stress-resistant solid state electrolyte for stable lithium-metal batteries, *Energy Storage Mater.*, 2022, **49**, 502–508.
10 Q. Liu, Y. Liu, X. Jiao, Z. Song, M. Sadd, X. Xu, A. Matic, S. Xiong and J. Song, Enhanced ionic conductivity and interface stability of hybrid solid-state polymer electrolyte for rechargeable lithium metal batteries, *Energy Storage Mater.*, 2019, **23**, 105–111.
11 Y. Du, S. Deng, Y. Zhu, J. Jiang, G. Yang, M. Wu and Z. Li, Advancements in polymer materials for high-energy-density lithium-ion batteries, *Chem. Soc. Rev.*, 2025, **54**, 8287–8324.
12 Z. Song, M. Tian, J. Zhu, J. Chen, W. Feng, L. Ben, H. Yu, X. Huang, M. Armand, Z. Zhou and H. Zhang, Super SEI-forming anion for enhanced interfacial stability in solid-state lithium metal batteries, *Adv. Mater.*, 2024, **36**, e2410954.
13 X. Zhang, H. Yu, L. Ben, G. Cen, Y. Sun, L. Wang, J. Hao, J. Zhu, Q. Sun, R. Qiao, X. Yao, H. Zhang and X. Huang, Topology fortified anodes powered high-energy all-solid-state lithium batteries, *Adv. Mater.*, 2025, **37**, e2506298.
14 J. Ma, Y. Zhu, H. Wang, Y. Zhang, Q. Wu, Z. Qin, J. Zhang, B. Liu, D. Huang, Y. Ren, C. W. Nan and X. Wang, Tuning anion chemistry to enhance bulk and interfacial stability in low-temperature lithium metal batteries, *Adv. Energy Mater.*, 2025, **15**, 2500631.
15 J. Zhang, J. Fu, P. Lu, G. Hu, S. Xia, S. Zhang, Z. Wang, Z. Zhou, W. Yan, W. Xia, C. Wang and X. Sun, Challenges and strategies of low-pressure all-solid-state batteries, *Adv. Mater.*, 2025, **37**, e2413499.
16 X. L. Wang, Y. Li, J. Liu, S. J. Yang, J. K. Hu, W. Q. Mai, R. Wen, H. Yuan and J. Q. Huang, A robust dual-layered solid electrolyte interphase enabled by cation specific adsorption-induced built-in electrostatic field for long-cycling solid-state lithium metal batteries, *Angew. Chem., Int. Ed.*, 2025, **64**, e202421101.
17 Y. Feng, Y. Fan, L. Zhao, J. Yu, Y. Liao, T. Zhang, R. Zhang, H. Zhu, X. Sun, Z. Hu, K. Zhang and J. Chen, Enhancing microdomain consistency in polymer electrolytes towards sustainable lithium batteries, *Angew. Chem., Int. Ed.*, 2025, **64**, e202417105.
18 X. Gong, J. Wang, L. Zhong, G. Qi, F. Liu, Y. Pan, F. Yang, X. Wang, J. Li, L. Li, C. Liu and D. Yu, Recent advances on cellulose-based solid polymer electrolytes, *Ind. Chem. Mater.*, 2025, **3**, 31–48.
19 X. Ma, J. Yu, Y. Hu, J. Texter and F. Yan, Ionic liquid/poly(ionic liquid)-based electrolytes for lithium batteries, *Ind. Chem. Mater.*, 2023, **1**, 39–59.
20 X. Jiao, Y. Wang, S. Xiong, X. Xu, Z. Song and Y. Liu, Electro-chemo-mechanical failure of solid-state electrolyte caused from intergranular or transgranular damage propagation in polycrystalline aggregates, *Acta Mater.*, 2024, **265**, 119607.
21 X. Jiao, Y. Wang, O. O. Kapitanova, X. Xu, V. S. Volkov, Y. Liu, Z. Song, A. Matic and S. Xiong, Morphology evolution of electrodeposited lithium on metal substrates, *Energy Storage Mater.*, 2023, **61**, 102916.
22 Y. Zheng, Y. Yao, J. Ou, M. Li, D. Luo, H. Dou, Z. Li, K. Amine, A. Yu and Z. Chen, A review of composite solid-state electrolytes for lithium batteries: Fundamentals, key materials and advanced structures, *Chem. Soc. Rev.*, 2020, **49**, 8790–8839.
23 X. Wu, W. Zhang, H. Qu, C. Guan, C. Li, G. Lu, C. Chang, Z. Lao, Y. Zhu, L. Nie and G. Zhou, An oriented design of a π-conjugated polymer framework for high-performance solid-state lithium batteries, *Energy Environ. Sci.*, 2025, **18**, 1835–1846.
24 T. Hou, D. Wang, B. Jiang, Y. Liu, J. Kong, Y. He, Y. Huang and H. Xu, Ion bridging enables high-voltage polyether electrolytes for quasi-solid-state batteries, *Nat. Commun.*, 2025, **16**, 962.
25 Y. Liu, X. Xu, M. Sadd, O. O. Kapitanova, V. A. Krivchenko, J. Ban, J. Wang, X. Jiao, Z. Song, J. Song, S. Xiong and A. Matic, Insight into the critical role of exchange current density on electrodeposition behavior of lithium metal, *Adv. Sci.*, 2021, **8**, 2003301.
26 Y. Liu, S. Xiong, J. Wang, X. Jiao, S. Li, C. Zhang, Z. Song and J. Song, Dendrite-free lithium metal anode enabled by separator engineering via uniform loading of lithiophilic nucleation sites, *Energy Storage Mater.*, 2019, **19**, 24–30.
27 M. Tian, R. Qiao, G. Cen, L. Tian, L. Ben, H. Yu, M. De Volder, C. Zhao, Q. Wang and X. Huang, Dual-gradient metal layer for practicalizing high-energy lithium batteries, *Nat. Commun.*, 2025, **16**, 6864.
28 G. Cen, H. Yu, R. Xiao, L. Ben, R. Qiao, J. Zhu, X. Zhang, G. Liu, K. Jiang, X. Yao, H. Zhang and X. Huang, Adaptive interphase enabled pressure-free all-solid-state lithium metal batteries, *Nat. Sustain.*, 2025, **8**, 1360–1370.
29 A. Masias, N. Felten, R. Garcia-Mendez, J. Wolfenstine and J. Sakamoto, Elastic, plastic, and creep mechanical properties of lithium metal, *J. Mater. Sci.*, 2018, **54**, 2585–2600.
30 Y. Chen, Z. Wang, X. Li, X. Yao, C. Wang, Y. Li, W. Xue, D. Yu, S. Y. Kim, F. Yang, A. Kushima, G. Zhang, H. Huang, N. Wu, Y. W. Mai, J. B. Goodenough and J. Li, Li metal deposition and stripping in a solid-state battery via Coble creep, *Nature*, 2020, **578**, 251–255.
31 Z. Wang, X. Li, Y. Chen, K. Pei, Y.-W. Mai, S. Zhang and J. Li, Creep-enabled 3D solid-state lithium-metal battery, *Chem*, 2020, **6**, 2878–2892.
32 S. Ren, Y. Su, W. Jiang, Y. Su and Y. Zhang, Influence of free space on lithium growth behavior at open surfaces and internal cracks of sulfide-based solid electrolyte, *Adv. Mater.*, 2025, **37**, 2414239.
33 M. J. Wang, R. Choudhury and J. Sakamoto, Characterizing the Li-solid-electrolyte interface dynamics as a function of stack pressure and current density, *Joule*, 2019, **3**, 2165–2178.
34 H. Yan, K. Tantratian, K. Ellwood, E. T. Harrison, M. Nichols, X. Cui and L. Chen, How does the creep stress regulate void formation at the lithium-solid electrolyte interface during stripping?, *Adv. Energy Mater.*, 2021, **12**, 2102283.
35 X. Han, Y. Gong, K. K. Fu, X. He, G. T. Hitz, J. Dai, A. Pearse, B. Liu, H. Wang, G. Rubloff, Y. Mo, V. Thangadurai, E. D. Wachsman and L. Hu, Negating interfacial impedance in garnet-based solid-state Li metal batteries, *Nat. Mater.*, 2017, **16**, 572–579.